RSC Advances

ROYAL SOCIETY OF CHEMISTRY

PAPER

View Article Online
View Journal | View Issue

Check for updates

Cite this: *RSC Adv.*, 2024, **14**, 650

Facile synthesis of morphology-controlled hybrid structure of $ZnCo_2O_4$ nanosheets and nanowires for high-performance asymmetric supercapacitors†

Huiqing Fan, *[a] Hexiang Di,[a] Yanlei Bi,[a] Ru Wang,[a] Guangwu Wen[b] and Lu-Chang Qin[c]

Controllable synthesis of electrode materials with desirable morphology and size is of significant importance and challenging for high-performance supercapacitors. Herein, we propose an efficient hydrothermal approach to controllable synthesis of hierarchical porous three-dimensional (3D) $ZnCo_2O_4$ composite films directly on Ni foam substrates. The composite films consisted of two-dimensional (2D) nanosheets array anchored with one-dimensional (1D) nanowires. The morphologies of $ZnCo_2O_4$ arrays can be easily controlled by adjusting the concentration of NH_4F. The effect of NH_4F in the formation of these 3D hierarchical porous $ZnCo_2O_4$ nanosheets@nanowires films is systematically investigated based on the NH_4F-independent experiments. This unique 3D hierarchical structure can help enlarge the electroactive surface area, accelerate the ion and electron transfer, and accommodate structural strain. The as-prepared hierarchical porous $ZnCo_2O_4$ nanosheets@nanowires films exhibited inspiring electrochemical performance with high specific capacitance of 1289.6 and 743.2 F g^{-1} at the current density of 1 and 30 A g^{-1}, respectively, and a remarkable long cycle stability with 86.8% capacity retention after 10 000 cycles at the current density of 1 A g^{-1}. Furthermore, the assembled asymmetric supercapacitor using the as-prepared $ZnCo_2O_4$ nanosheets@nanowires films as the positive electrode and active carbon as negative electrode delivered a high energy density of 39.7 W h kg^{-1} at a power density of 400 W kg^{-1}. Our results show that these unique hierarchical porous 3D $ZnCo_2O_4$ nanosheets@nanowires films are promising candidates as high-performance electrodes for energy storage applications.

Received 19th October 2023
Accepted 8th December 2023

DOI: 10.1039/d3ra07128f

rsc.li/rsc-advances

1. Introduction

Because of the impending energy crisis coupled with the immoderate exhaustion of fossil fuels, searching for sustainable and high-performance renewable energy storage and conversion devices is one of the most imminent challenges facing us today.[1–3] Supercapacitors, as promising energy storage devices with high power density, fast recharge capability, long cycling life, and environmental compatibility, have aroused considerable attention and been widely applied to high power portable electronics and hybrid electric vehicles.[4,5] However, supercapacitors still have unsatisfactory energy densities, which are usually an order of magnitude lower than lithium-ion batteries. Therefore, a crucial task in the research and development of supercapacitors is to further improve their energy density without sacrificing their high power density.[6] According to the expression of energy density, $E = \frac{1}{2}CV^2$, in which C is the specific capacitance and V is the working voltage of the supercapacitor, two effective approaches have earned foremost attention to increase the energy density of supercapacitors: (1) developing new electrode materials with enhanced specific capacitance (C), and/or (2) constructing asymmetric supercapacitors to broaden the operating voltage window (V).[7,8] To meet the challenges, developing suitable electrode materials with appealing electrochemical performance is imperative to fulfill the above two approaches for further enhancing the energy density performance of supercapacitors.

In recent years, compared with cobalt oxides, ternary cobalt-based metal oxides (such as $ZnCo_2O_4$, $NiCo_2O_4$) have evoked increasing attention as efficient electrode materials for supercapacitors because of their excellent intrinsic properties, originating from the synergistic effects between two different metal

---

[a] *School of Chemistry and Chemical Engineering, Shandong University of Technology, Zibo, China. E-mail: huiqingfan@yeah.net; hqfan@sdut.edu.cn*

[b] *School of Materials Science and Engineering, Shandong University of Technology, Zibo, China*

[c] *Department of Physics and Astronomy, University of North Carolina at Chapel Hill, Chapel Hill, NC 27599-3255, USA*

† Electronic supplementary information (ESI) available. See DOI: **https://doi.org/10.1039/d3ra07128f**

ions during the faradaic redox reactions.[9–11] Among them, $ZnCo_2O_4$ has been widely investigated due to its high theoretical specific capacitance (2604 F g^{-1}), rich redox reactions, and morphological diversity.[12–15] Until recently, nanostructured $ZnCo_2O_4$ materials with various morphologies have been synthesized by diversified routes and applied as supercapacitor electrode materials, such as nanoparticles,[15] nanowires,[13] nanosheets,[16] and nanoflowers.[17] Despite these inspiring reports, the nanostructured $ZnCo_2O_4$ materials still suffer from low-rate performance and poor cycling stability due to the serious self-aggregation during the repeated discharging-charging process because of their high surface area and energy, as well as low packing density results in a low volumetric energy density.

Several strategies have been adopted to enhance the electrochemical kinetics as well as mechanical stability of the $ZnCo_2O_4$ materials. An effective approach is to design and synthesize controllably hierarchical porous three-dimensional (3D) micro/nanostructured $ZnCo_2O_4$ materials, as they endow the superiority of both the nanoscale building blocks and the microscale secondary architectures. This unique 3D hierarchical structure is favorable to enhance the electroactive surface area, accelerate the ion and electron transfer, and accommodate structural strain. These factors are responsible for the enhanced electrochemical kinetics and cycling stability.[18,19] Recently, extensive research efforts have been made to controllably synthesize various hierarchical 3D $ZnCo_2O_4$ micro/nanostructure materials. For example, Du *et al.* succeeded in preparing $ZnCo_2O_4$ with different morphologies by adding template agent CTAB, PVA, PVP, and SDS and the flower-like $ZnCo_2O_4$ electrode prepared using PVP exhibited superior performance with a high specific capacitance of 1527.2 and 1204 F g^{-1} at the current density of 1 and 10 A g^{-1}, respectively.[20] Chen *et al.* successfully synthesized hierarchical $ZnCo_2O_4$ microspheres utilizing ethylene glycol as the structure-directing, and the results indicated that a high specific capacitance of 689 F g^{-1} at 1 A g^{-1} and a good rate capability of 81.3% capacitance retention at 15 A g^{-1} could be achieved.[21] Among these strategies, surfactants or polymers are added as structure-directing reagents to better control over the morphology and size of the 3D $ZnCo_2O_4$ micro/nanostructure materials. Whereas, such additives are usually high-cost, environment-hazardous, and difficult to remove. Controllable synthesis of $ZnCo_2O_4$ with well-defined 3D hierarchical micro/nanostructured architecture using an appropriate inorganic soluble salt as the chelating agent or morphology controlling agent is still an unsolved big issue in the research and development of supercapacitors.

On the other hand, when the traditional template method is used for the synthesis of 3D micro/nanostructured $ZnCo_2O_4$ materials, it requires a tedious process of mixing carbon blacks and polymeric binders with the active materials.[22] Such additives not only impede the electrons/ions transport due to the "dead surface", but also undermine the entire energy storage capacity. Therefore, it is of vital significance to develop a highly efficient and simple synthetic strategy for controllable synthesis of self-supporting 3D micro/nanostructured $ZnCo_2O_4$ materials directly on conductive substrates.

In this work, we propose a facile and efficient hydrothermal approach to the controllable synthesis of 3D hierarchical $ZnCo_2O_4$ nanosheets@nanowires arrays directly on Ni foam by simply tuning the amount of NH_4F as a morphology controlling agent. The effect of NH_4F during the synthesis was systematically investigated and analyzed. Electrochemical performance of the as-prepared 3D hierarchical $ZnCo_2O_4$ nanosheets@nanowires electrodes was also investigated in detail. A remarkable specific capacitance of 1289.6 F g^{-1} was achieved at the current density of 1 A g^{-1} and the specific capacitance could also be maintained at 743.2 F g^{-1} even at 30 A g^{-1}. Furthermore, an asymmetric supercapacitor (ASC) device was assembled using the as-prepared $ZnCo_2O_4$ materials and active carbon (AC) as positive and negative electrode, respectively, in order to further evaluate its practical applications. The $ZnCo_2O_4$//AC ASC exhibited an excellent energy density of 39.7 W h kg^{-1} at a high power density of 400 W kg^{-1}, and a superior cycling stability (71.4% capacity retention after 10 000 cycles at 1 A g^{-1}). The enhanced electrochemical properties are ascribed to the unique structural merits, such as large electroactive surface area, hierarchical porous structure, decent structural stability, excellent conductivity, and strong connections between the $ZnCo_2O_4$ active materials and the substrate. These results show that such 3D hierarchical $ZnCo_2O_4$ nanosheets@nanowires materials can be a promising candidate for applications in high-performance energy storage devices.

2. Experimental

2.1 Synthesis of $ZnCo_2O_4$ material

All the chemical reagents used in this study are of analytical purity without further purification. Before synthesis, the Ni foam (1 × 4.5 cm^2) was pretreated sequentially with acetone, 3 M HCl solution, ethanol, and deionized water for 10 min each to obtain a clean surface.

In a typical procedure, 10 mmol of $ZnSO_4\cdot 7H_2O$, 20 mmol of $CoSO_4\cdot 7H_2O$, 40 mmol of ammonium fluoride (NH_4F), and 125 mmol of urea were dissolved in 150 mL of deionized water to form a pink transparent solution. The above solution was transferred into a 30 mL Teflon-lined stainless steel autoclave and a piece of pretreated Ni foam with an exposed area of 1 × 2 cm^2 (the other section was protected from solution contamination by uniformly coating with a polytetrafluoroethylene tape) was immersed into the reaction solution. Afterwards, the autoclave was held at 120 °C for 5 h and then allowed to cool naturally to room temperature. Then, the Ni foam loaded with precursor was collected, cleaned with deionized water and ethanol several times, and dried at 60 °C for 8 h. Finally, the as-prepared precursor was annealed at 300 °C for 3 h in air with a heating rate of 2 °C min^{-1}.

2.2 Materials characterization

The surface morphology and microstructure of the as-prepared materials were characterized by field-emission scanning electron microscopy (FE-SEM, Gemini 300-71-31) and transmission electron microscopy (TEM, FEI Tecnai F20). The crystal structure was analyzed by X-ray diffraction (XRD, Shimadzu 7000) with Cu K_α radiation in the angular range of 5–90° at 40 kV/30 mA. Raman spectra were recorded using a HORIBA LabRAM HR Evolution with an excitation wavelength of 514 nm. The chemical composition and elemental valence were analyzed with X-ray photoelectron spectroscopy (XPS, Thermo Kalpha, Thermo ESCALAB 250XI). The energy dispersive X-ray spectroscopy (EDS) was carried out on field-emission scanning electron microscopy (FESEM, Gemini, 300-71-31). The specific surface area, pore volume and pore-size distributions were analyzed by a N_2 adsorption–desorption measurement (NOVA 2200e) using the Brunauer–Emmett–Teller (BET) method and Barrett–Joyner–Halenda (BJH) model, respectively.

2.3 Electrochemical measurements

Electrochemical measurements were evaluated in a conventional three-electrode system with 6 M KOH aqueous solution as the electrolyte. The as-prepared $ZnCo_2O_4$ grown on Ni foam was used directly as the working electrode. An Ag/AgCl electrode and a platinum foil were used as the reference and counter electrode, respectively. Cyclic voltammetry (CV) tests were conducted at various scan rates using a CHI660E electrochemical workstation. Galvanostatic charge–discharge (GCD) measurements were measured within the potential range of 0–0.35 V at different current densities. Electrochemical impedance spectroscopy (EIS) measurements were performed over the frequency range from 100 kHz to 0.01 Hz at the open circuit potential.

The specific capacitance (C_s, F g^{-1}) of the as-prepared $ZnCo_2O_4$ electrodes can be calculated by the following formula:

$$C_s = \frac{I \times \Delta t}{m \times \Delta V} \tag{1}$$

where I (A) is the constant discharge current, Δt (s) is the discharge time, m (g) is the mass of the active material, and ΔV (V) is the window potential upon discharging.

2.4 Fabrication of $ZnCo_2O_4$//AC asymmetric supercapacitor

To fabricate the asymmetric supercapacitor device, the as-prepared $ZnCo_2O_4$ films as the positive electrode and active carbon as the negative electrode with the cellulose paper as the separator, assembling into a coin cell CR2025 in 6 M KOH electrolyte. The mass ratio between the $ZnCo_2O_4$ positive electrode and the active carbon negative electrode was determined by the charge balance theory ($q^+ = q^-$) using the following equation:

$$\frac{m_+}{m_-} = \frac{C_- \times \Delta V_-}{C_+ \times \Delta V_+} \tag{2}$$

where m (g) is the mass of active material, C (F g^{-1}) is the specific capacitance, and ΔV (V) is the potential range for positive and negative electrodes, respectively.

The specific capacitance (C_s, F g^{-1}), energy density (E, W h kg^{-1}) and power density (P, W kg^{-1}) of the asymmetric supercapacitor were calculated according to the following equations:

$$C_s = \frac{I \times \Delta t}{m \times \Delta V} \tag{3}$$

$$E = \frac{1}{2} \times C_s \times \Delta V^2 \tag{4}$$

$$P = E/\Delta t \tag{5}$$

where I (A) is the constant discharge current, Δt (s) is the discharge time, m (g) is the total mass of the two electrodes, ΔV (V) is the potential window of the device.

3. Results and discussion

The crystal structure and phase purity of the as-prepared films were characterized by XRD. Fig. 1a shows the XRD pattern of the as-prepared films exfoliated from the surface of Ni foam to avoid excessive peak intensity due to Ni on the diffractogram. The diffraction peaks at 18.98°, 31.14°, 36.72°, 37.98°, 44.82°, 59.46°, and 64.92° are due to crystal lattice planes (111), (220), (311), (222), (400), (511), and (440) of the spinel phase of $ZnCo_2O_4$ (JCPDS file 23-1390).[23] No contaminant such as Co_3O_4 or ZnO was observed in the XRD pattern, indicating a high purity of the $ZnCo_2O_4$ phase. The atomic ratio of Zn and Co was approximately 1 : 2 as revealed by EDS (Fig. S1†), which showed the successful synthesis of $ZnCo_2O_4$, in agreement with the XRD analysis. Fig. 1b presents the Raman spectra of the as-prepared films. The peak at 188 cm^{-1} ($F_{2g}^{(3)}$ mode) corresponds to A–O stretching mode in AB_2O_4 spinels, which is mainly attributed to Co ions in tetrahedral sites of Co_3O_4.[19] The peaks located at 477 and 521 cm^{-1} have the E_g and $F_{2g}^{(2)}$ symmetry, respectively. The weak peak located at 611 cm^{-1} is assigned to the $F_{2g}^{(1)}$ symmetry. The band at 677 cm^{-1} (A_{1g} mode) belongs to the B–O stretching mode in AB_2O_4 spinels.[24] This result further confirms the successful synthesis of $ZnCo_2O_4$ films.

The chemical composition and oxidation valence state of the as-prepared films were analyzed by XPS and the corresponding results are displayed in Fig. 2. The wide-scan XPS spectrum in Fig. 2a confirms the presence of Co, Ni, Zn, O, and C in the sample. The presence of Ni resulted from the nickel foam substrate and the C 1s peak at 284.6 eV is used as the reference for calibration. Fig. 2b displays the high-resolution Zn 2p XPS spectrum. Two major peaks at 1044.4 eV for Zn $2p_{1/2}$ and 1021.3 eV for Zn $2p_{3/2}$ are observed, indicating the Zn(II) oxidation state of $ZnCo_2O_4$.[25] The two peaks at binding energies of 795.2 and 779.8 eV in the Co 2p XPS spectrum (Fig. 2c) are attributed to the characteristic Co $2p_{1/2}$ and Co $2p_{3/2}$, respectively. The resolved peaks at 779.6 and 794.8 eV are attributed to the Co^{3+} state.[26] Furthermore, the peaks at 781.2 and 796.5 eV are assigned to the Co^{2+} state,[27] indicating the coexistence of Co(II) and Co(III). As shown in Fig. 2d, the O 1s spectrum can be deconvoluted into two oxygen contributions (O_I and O_{II}). The O_I component observed at 529.4 eV is attributed to metal–oxygen bonding (O bonding with Co or Zn).[28] The O_{II} peak at 532.0 eV corresponds to the physically and chemically adsorbed water on

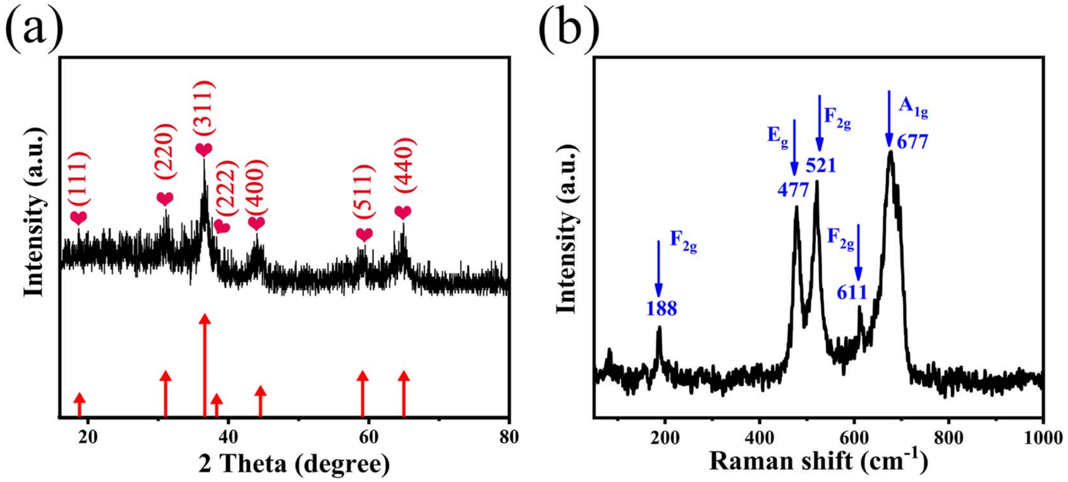

Fig. 1 (a) XRD pattern and (b) Raman spectra of the 3D hierarchical $ZnCo_2O_4$ nanosheets@nanowires films.

the surface of $ZnCo_2O_4$.[21] The above results confirmed again the formation of $ZnCo_2O_4$ films on Ni foam.

The SEM images of the $ZnCo_2O_4$ films synthesized on Ni foam are shown in Fig. 3. As revealed in the low magnification SEM image (Fig. 3a), the hierarchical $ZnCo_2O_4$ nanosheets@nanowires hybrid structures covered uniformly and densely the 3D Ni foam substrate. As the backbone, the 2D $ZnCo_2O_4$ nanosheets lie aslant or perpendicular to the substrate

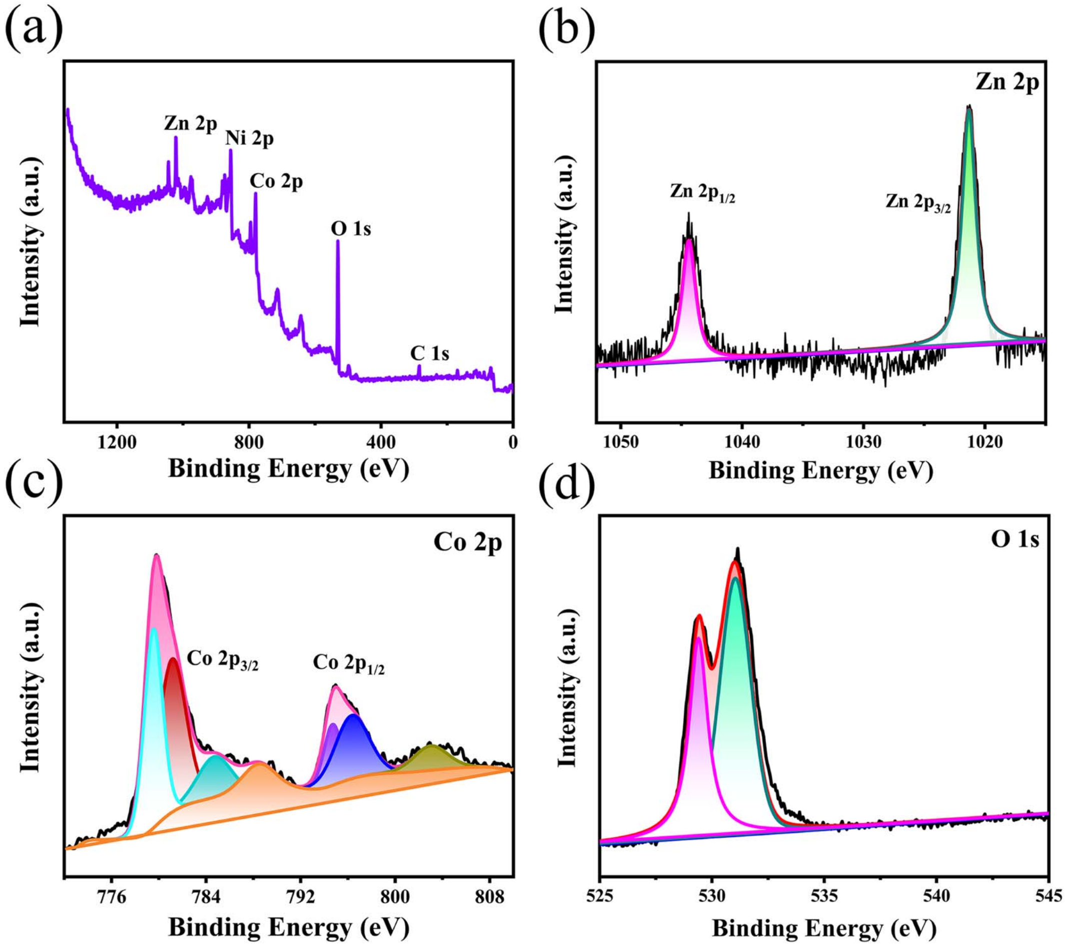

Fig. 2 XPS spectra of the 3D hierarchical $ZnCo_2O_4$ nanosheets@nanowires films: (a) wide-scan, (b) Zn 2p, (c) Co 2p and (d) O 1s spectrum.

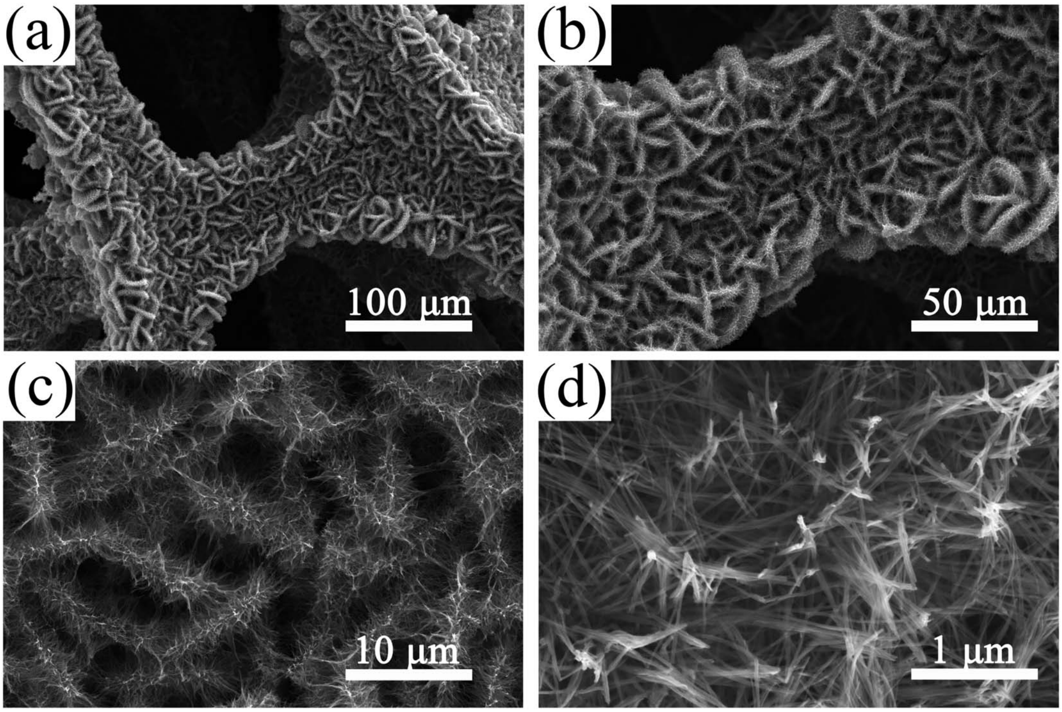

Fig. 3 SEM images of the 3D hierarchical $ZnCo_2O_4$ nanosheets@nanowires films on Ni foam at different magnifications.

and they are interconnected and intercrossed with each other, forming ordered nanosheet arrays with an open porous network structure that can provide great surface area between the electrode and electrolyte (Fig. 3b). As shown in the high magnification SEM image (Fig. 3c), the well-resolved nanowires are grown vertically on the interconnected nanosheets. The nanowires have a typical length of ~1 μm and diameter of ~30 nm, as shown in Fig. 3d. It is worth noting that these unique 3D nanosheets@nanowires hybrid structures could not only provide a better mechanical strength, but should also form a hierarchical porous architecture for fast ion diffusion and transport, thus facilitating the enhancement of electrochemical performance.

To further view the detailed structure of the as-prepared $ZnCo_2O_4$ films, TEM characterization was employed. The low-magnification TEM images (Fig. 4a and b) reveal that the microstructure of $ZnCo_2O_4$ is composed by nanosheets and nanowires, which is in agreement with the SEM observations. TEM image in Fig. 4c confirmed the diameter of 1D nanowires is ~30 nm and the nanowire is composed of a large number of nanoparticles. Moreover, the formation of porous structure in the nanowires is due to the release of H_2O and reaction gases from the Zn–Co precursors during the calcination process. Fig. 4d shows a high-resolution TEM image (HRTEM) taken from the selected area, in which the lattice spacing of 0.24 nm and 0.29 nm are ascribed to the (311) and (220) crystal lattice planes of $ZnCo_2O_4$, respectively. Fig. 4e gives the selected-area electron diffraction (SAED) pattern with sharp Bragg reflections, in good agreement with the XRD analysis shown in Fig. 1a. The elemental distribution was investigated through energy dispersive X-ray spectroscopy (EDS) mapping. The corresponding results (Fig. 4f–i) clearly revealed that the Co, Zn and O components are distributed homogeneously within the entire structure, confirming the successful synthesis of hierarchical porous 3D $ZnCo_2O_4$ nanosheets@nanowires.

The N_2 adsorption–desorption measurement was used to obtain the specific surface area and pore size distribution of the as-prepared $ZnCo_2O_4$ films and the results are shown in Fig. 5. Fig. 5a shows the N_2 adsorption–desorption isotherms, where a typical IV isotherm with a distinct H_3 hysteresis loop is observed.[29] According to the Brunauer–Emmett–Teller (BET) theory, the calculated specific surface area of the as-prepared $ZnCo_2O_4$ sample is 21.52 $m^2\ g^{-1}$. The Barrett–Joyner–Halenda (BJH) pore size distribution is shown in Fig. 5b. It is clearly shown that the pore size is mainly distributed in the range of 38–42 nm, confirming the mesoporous structure of the $ZnCo_2O_4$ sample, which enhanced the diffusion of electrolyte ions during electrochemical reactions that could further improve the electrochemical performance of the $ZnCo_2O_4$ electrode.

In our work, we found that the amount of NH_4F played a key role in the formation of such hierarchical macro/nanostructures. Therefore, in order to further understand the relationship between the amount of NH_4F in reactions and the material morphologies, the morphological evolution of the as-prepared $ZnCo_2O_4$ films with various amounts of NH_4F was investigated. The related results are shown in Fig. 6. It is clearly observed that the morphology of the as-prepared $ZnCo_2O_4$ films experienced evident changes with the gradual increase of NH_4F. Without assistance from NH_4F, the disordered clusters of nanosheets with a wide size distribution can be observed in

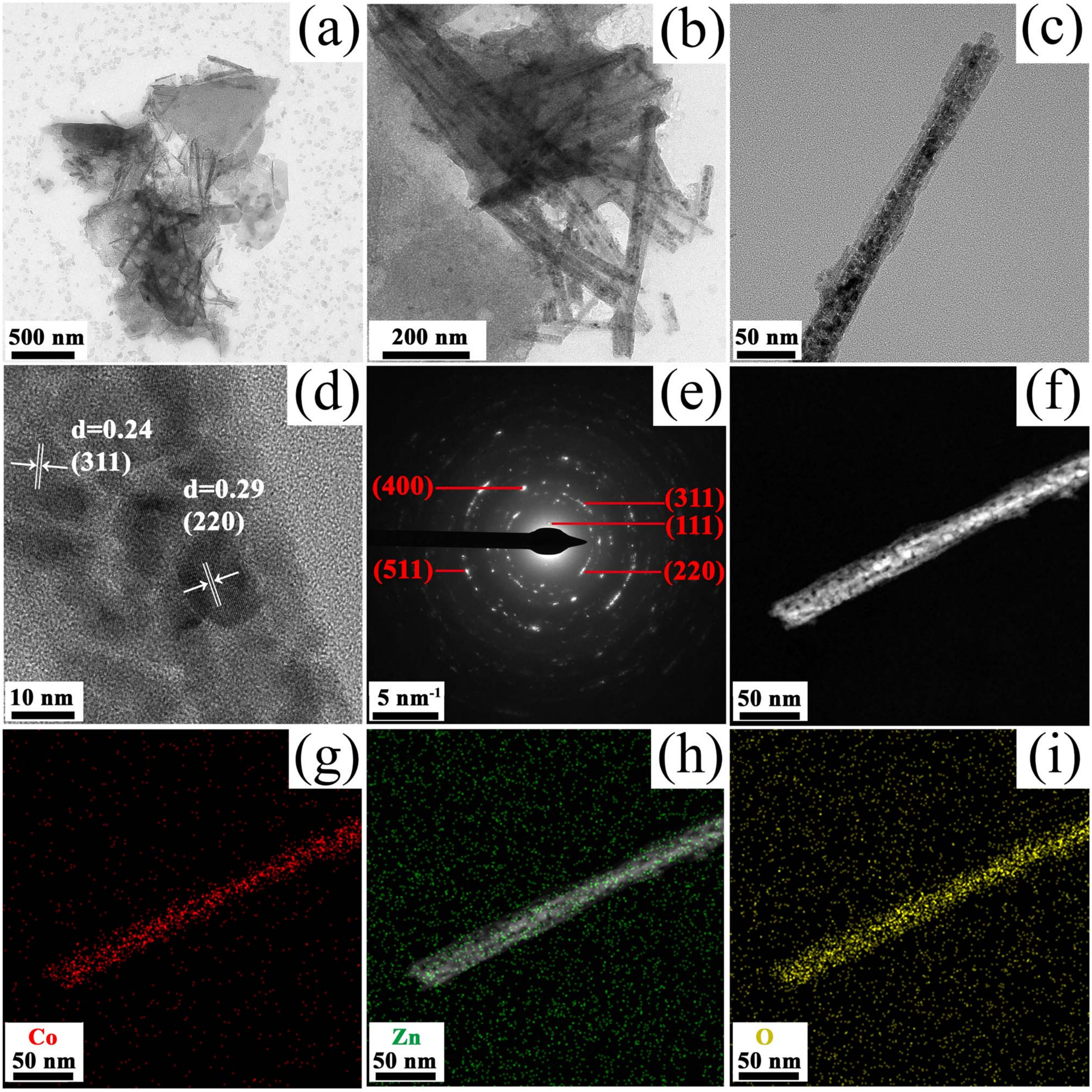

Fig. 4 (a–c) TEM images of the 3D hierarchical $ZnCo_2O_4$ nanosheets@nanowires films at different magnifications. (d) HRTEM image and (e) SAED pattern of the 3D hierarchical $ZnCo_2O_4$ nanosheets@nanowires films. (f–i) Elemental mapping images of the Co, Zn, and O of the 3D hierarchical $ZnCo_2O_4$ nanosheets@nanowires films.

Fig. 6a–c. When the concentration of NH_4F increased to 20 mmol, ordered nanosheets were intercrossed and interconnected to each other (Fig. 6d and e) and dense nanowires were formed on the surface of nanosheets (Fig. 6f). In the meanwhile, the nanosheets with a larger lateral size showed a loose architecture, which is different from the material obtained with 40 mmol NH_4F. Compared to the nanosheet structure without NH_4F, the obtained structure (with 20 mmol NH_4F) was prone to becoming more ordered. When the concentration of NH_4F was adjusted to 40 mmol, it was observed, as shown in Fig. 3, that a highly ordered hierarchical nanosheets@nanowires architecture was formed. However, when the concentration of NH_4F was further increased to 50 mmol, the nanosheets almost disappeared and the top-converged nanowires appeared instead, forming a compact and dense film, which is not conducive to the electrochemical reactions (Fig. 6g–i). Based on the above experimental results, we conclude that a moderate amount of NH_4F can promote the formation of well-defined hierarchical nanosheets@nanowires.

To further interpret the morphological evolution described above, the three functions of F^- in the fabrication process are summarized as follows: (1) activation of Ni foam substrate:[30,31]

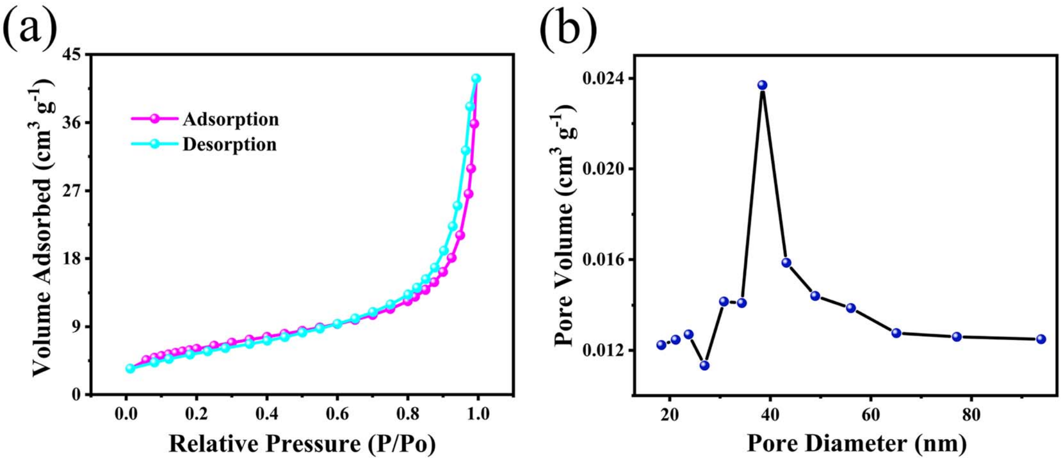

Fig. 5 (a) N_2 adsorption–desorption isotherms and (b) pore size distribution curve of the 3D hierarchical $ZnCo_2O_4$ nanosheets@nanowires films.

After introducing NH_4F, the Ni foam substrate is activated, thus producing more active sites for nucleation and growth of the active material, as well as benefiting a compact adhesion between the active material and the substrate; (2) coordination between F^- and metal cations (Co^{2+} and Zn^{2+}):[32,33] when NH_4F is introduced, the coordination of metal cations with F^- should be taken into consideration. The reactions would reduce the concentration of free metal cations, which would further reduce the nucleation rate of the $ZnCo_2O_4$ precursor; (3) ionic hydration:[34] when NH_4F is added, the water molecules in the solution would be bounded around F^- as a result of ionic hydration of F^-. The ionic hydration effect would inhibit the movement of water molecules, resulting in an increase of the average activity coefficient of the ions in the solution and further increasing the nucleation and growth rate of the $ZnCo_2O_4$ precursor.

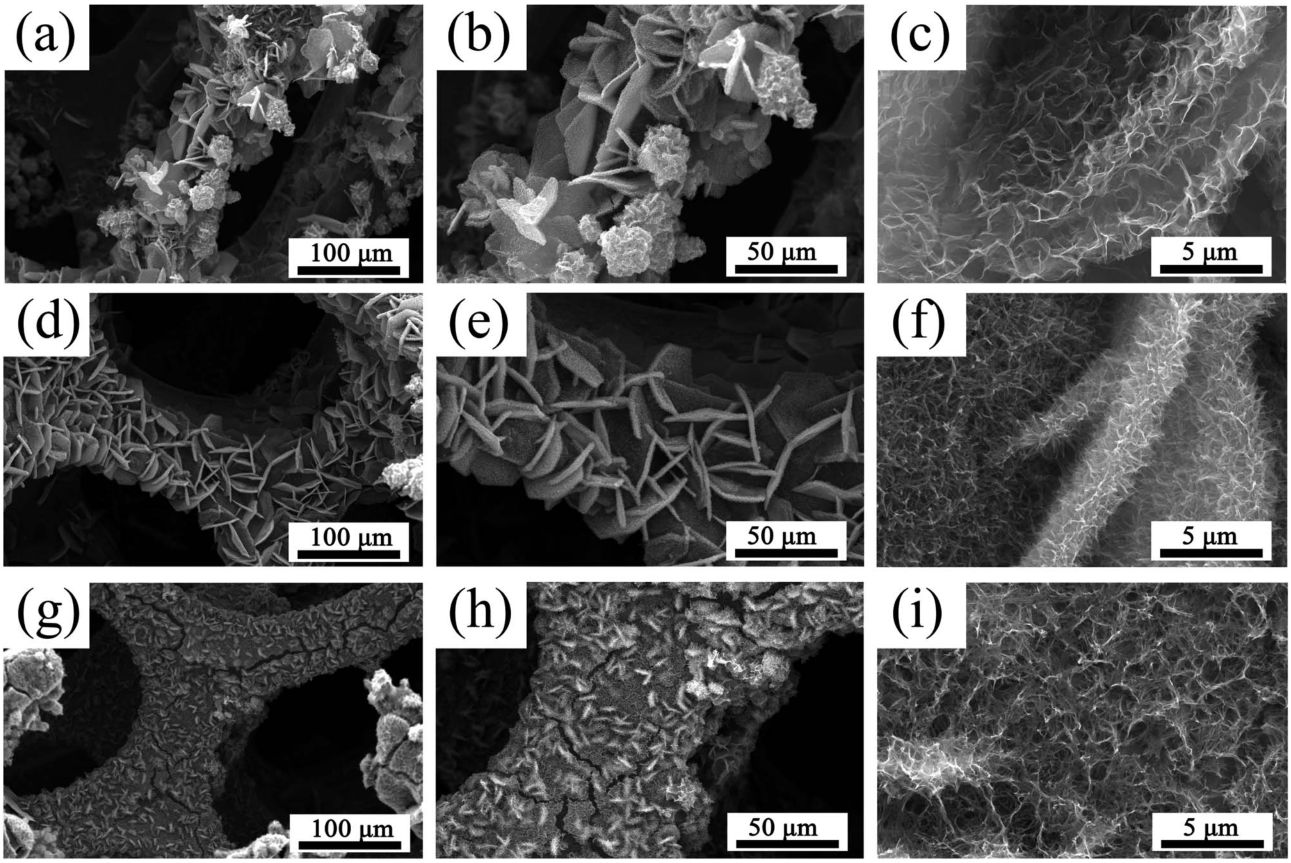

Fig. 6 SEM images of the $ZnCo_2O_4$ films obtained at different concentration of NH_4F: (a–c) without NH_4F, (d–f) 20 mmol NH_4F, (g–i) 50 mmol NH_4F.

In this work, the growth kinetics during the synthetic process is regarded as the synergistic effects of above three effects, which will control the morphologies of the final products. According to the analysis of morphological evolutions, it is clear that the reaction rate during the hydrothermal process played an essential role in the formation of samples with various morphologies. Based on the above experimental results and analyses, the corresponding mechanism for the effect of NH_4F concentration on the morphology of $ZnCo_2O_4$ samples is proposed and illustrated in Scheme 1. When NH_4F (20 mmol) is introduced, the presence of F^- can activate the substrate to produce more active sites for nucleation and growth, thus making nanosheets intercrossed and interconnected to each other to form a more ordered structure. This indicates that NH_4F plays a key role in regulating the morphology of the product. With a medium NH_4F concentration (40 mmol), the $ZnCo_2O_4$ precursor nanosheets have a smaller lateral size with a dense hierarchical architecture. The reason is suggested as follows: with a low NH_4F concentration, the ionic hydration effect of F^- could be neglected and the coordination between metal ions and F^- would reduce the concentration of free metal cations, leading to a slow reaction rate. The slow reaction rate could lead to the creation of nanosheets of larger lateral size with favored energetics, which can be explained by the Ostwald ripening.[35] On the other hand, with a medium NH_4F concentration, the ionic hydration effect of F^- has to be taken into consideration, which will increase the reaction rate. The fast growth rate contributed to the formation of nanosheets with a smaller lateral size, consequently forming a dense hierarchical architecture. Finally, with a high NH_4F concentration (50 mmol), the excessive F^- will destruct the hierarchical structure and form top-gathered nanowires, which is similar to the "coalescence growth" mechanism reported previously.[36] In summary, the controllable synthesis of $ZnCo_2O_4$ with various morphologies is regarded as kinetics controlled by the NH_4F concentration.

The as-prepared hierarchical porous 3D $ZnCo_2O_4$ nanosheets@nanowires films directly grown on Ni foam were directly used as the electrode for electrochemical evaluations without any further auxiliary treatment. Fig. 7a shows the cyclic voltammetry (CV) curves of the as-prepared $ZnCo_2O_4$ electrode over the potential range of −0.4–0.6 V at various scan rates. All the CV curves show a pair of well-defined redox peaks, corresponding to the typical reversible faradaic redox reactions.[37] With increasing the scan rates, the peak current density clearly increases and the anodic and cathodic peaks are systematically shifted to higher and lower potentials, respectively, due to the fast and reversible redox reactions between the electrode and the electrolyte interface.[38] Notably, it is shown in Fig. S2a† that the 3D $ZnCo_2O_4$ nanosheets@nanowires electrode shows a much larger redox peak area than the other three $ZnCo_2O_4$ film electrodes (with 0, 20, 50 mmol NH_4F), demonstrating its enhanced pseudocapacitive performance.

The galvanostatic charge–discharge (GCD) measurements of the as-prepared $ZnCo_2O_4$ electrode are further performed within the potential range of 0–0.35 V at different current densities ranging from 1 to 30 A g^{-1}, which is shown in Fig. 7b. All the GCD curves are nonlinear, confirming the pseudocapacitive behavior of the active material, which is in good agreement with the CV results.[39] Moreover, all the GCD curves are highly symmetrical without an obvious *IR* drop, demonstrating an excellent electrochemical reversibility and rapid IV response. The specific capacitance of the as-prepared $ZnCo_2O_4$ electrode is calculated from the GCD curves at various current densities and the obtained results are plotted in Fig. 7c. The calculated specific capacitance is 1289.6, 1247.7, 1216.6, 1171.1, 1087.7, 942.9, and 743.2 F g^{-1} at the current densities of 1, 2, 3, 5, 10, 20, and 30 A g^{-1}, respectively, demonstrating a good rate capability of the as-prepared $ZnCo_2O_4$ electrode. By comparing the results given in Fig. 7b, c and S2b, c,† it is found that the 3D $ZnCo_2O_4$ nanosheets@nanowires electrode displays larger specific capacitance than other $ZnCo_2O_4$ film electrodes (with 0, 20, 50 mmol NH_4F) at all the tested current densities.

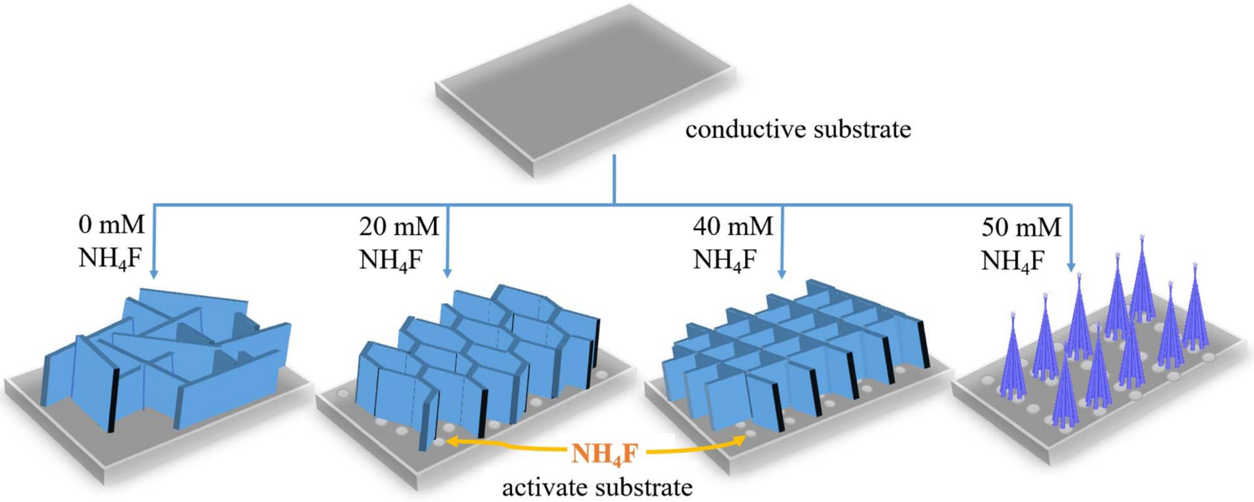

Scheme 1 Schematic illustrations of the mechanism for the effect of NH_4F on the morphology of $ZnCo_2O_4$ samples.

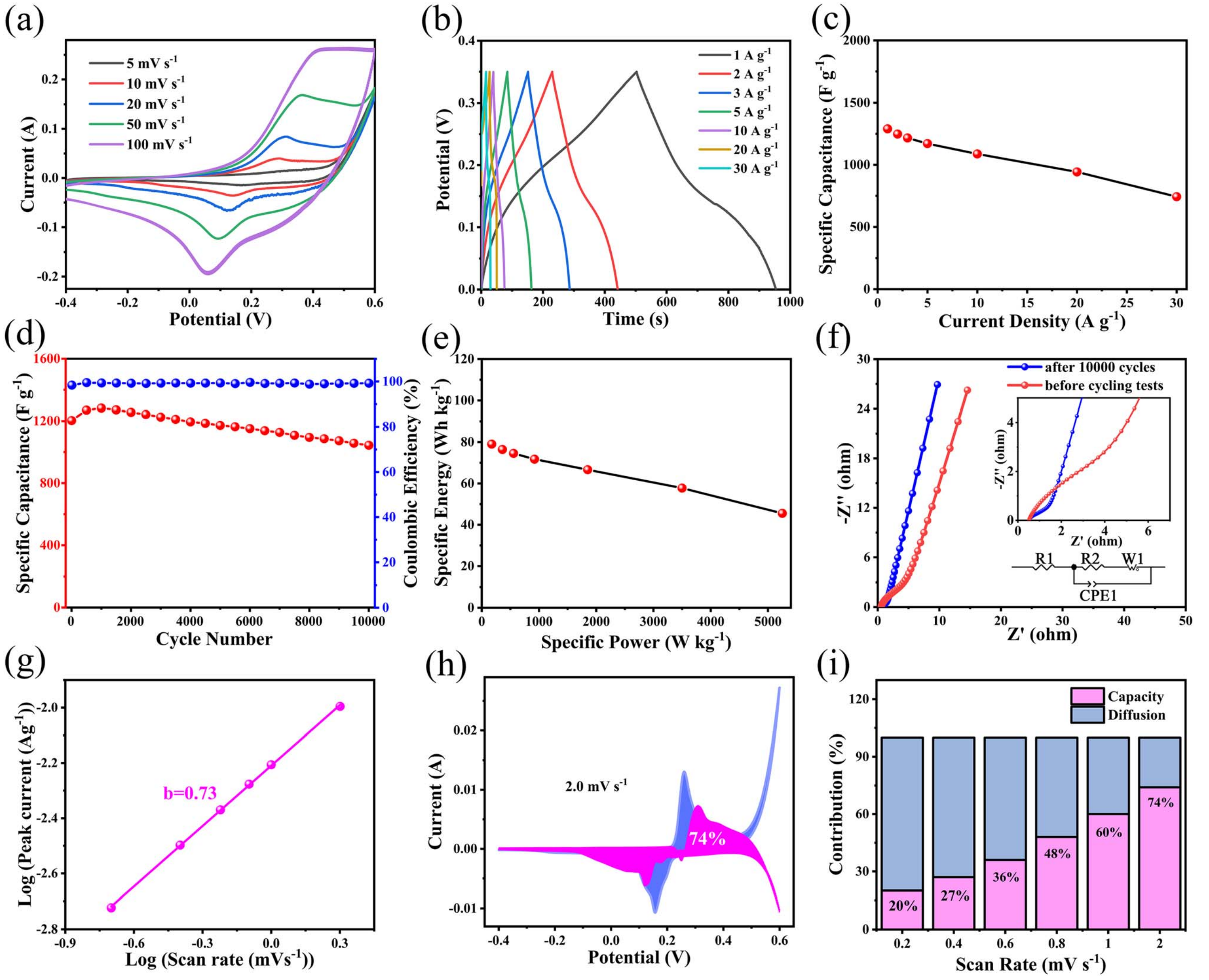

Fig. 7 Electrochemical properties of the 3D hierarchical $ZnCo_2O_4$ nanosheets@nanowires electrode. (a) CV curves at different scan rates (5–100 mV s^{-1}). (b) Galvanostatic charge–discharge curves at different current densities (1–30 A g^{-1}). (c) Specific capacitance at different current densities (1–30 A g^{-1}). (d) Cycling stability and coulomb efficiency at 1 A g^{-1}. (e) The Ragone plot related to energy and power densities. (f) Nyquist plots at open circuit state before and after 10 000 cycles, with the inset showing the enlarged high-frequency region and the corresponding equivalent circuit. (g) Straight line relationship of log(*i*) and log(*v*). (h) Separation of the diffusion- and capacitive-controlled currents of the 3D hierarchical $ZnCo_2O_4$ nanosheets@nanowires electrode at 2.0 mV s^{-1}. (i) The proportions of capacitive and diffusion controlled contribution at different scan rates.

The long cycling stability of the as-prepared $ZnCo_2O_4$ electrode is investigated by the continuous charge–discharge measurements at current density of 1 A g^{-1}, as shown in Fig. 7d. It was found that the specific capacitance increased within the initial 1000 cycles, attributed to the activation process that enhanced the participated electroactive surface areas.[40] Then, the specific capacitance exhibited a slow decrease until 10 000 cycles. After 10 000 cycles, 86.8% of the initial capacitance was retained with a coulombic efficiency of over 99.5%. As shown in Fig. 7d and S2d,† the 3D $ZnCo_2O_4$ nanosheets@nanowires electrode exhibits a much higher capacitance than the other $ZnCo_2O_4$ film electrodes (with 0, 20, 50 mmol NH_4F) during the whole electrochemical cycling process.

Electrochemical impedance spectroscopy (EIS) measurements were carried out to further determine the charge transfer kinetics of the as-prepared $ZnCo_2O_4$ electrode. Fig. 7f shows the Nyquist plots of the as-prepared $ZnCo_2O_4$ electrode before and after 10 000 cycles within the frequency ranging from 100 kHz to 0.01 Hz at the open circuit potential. It is clearly seen that, a semicircle at high frequency region and a straight line at low frequency region are present in all Nyquist plots. The intercept of the plots on the horizontal axis in the high frequency region gives the ohmic resistance (R_s), which is a combination of the ionic resistance of electrolyte, the intrinsic resistance of the $ZnCo_2O_4$ active material, and the contact resistance of the $ZnCo_2O_4$ active material and the current collector. The semicircle at high frequency region is attributed to the faradaic charge transfer resistance (R_{ct}) in parallel with the double layer capacitance. The straight line at low frequency region corresponds to the Warburg resistance. The equivalent circuit according to the above Nyquist plots is shown in the inset of Fig. 7f and the values of the fitting parameters are given in Table S1 in ESI.† Notably, R_s increased from 0.49 to 0.51 Ω, and R_{ct} increased from 0.29 to 1.92 Ω after 10 000 cycling, indicating that the resistance changed very little. These data indicate a low internal resistance, high electrical conductivity, and high adhesion of the as-prepared $ZnCo_2O_4$ electrode, which may account for the high cycling stability and enhanced rate capability.

To better investigate the kinetic behavior and charge storage mechanism of the as-prepared $ZnCo_2O_4$ electrode, the relationship between peak current (i) and scan rate (v) was analyzed according to the following equation:[41]

$$i = av^b \tag{6}$$

where a and b are adjustable constants. Specifically, the b value of 1 demonstrates the capacitive-controlled process, while the b value of 0.5 signifies the diffusion-controlled process. Fig. 7g shows the fitting line of log(i) *versus* log(v), the b value of anodic peak is calculated to be 0.73, suggesting that the charge storage process is the co-existence of the diffusion- and capacitive-controlled processes. Furthermore, the contributions of capacitive and diffusion-controlled process can be calculated according to the following equation:[42]

$$i = k_1v + k_2v^{1/2} \tag{7}$$

where k_1 and k_2 are adjustable constant. Fig. 7h presents that 74% of the entire capacity is regarded as the capacitive-controlled contribution at a scan rate of 2.0 mV s^{-1}. As displayed in Fig. 7i, the capacitive-controlled contribution of the as-prepared $ZnCo_2O_4$ electrode is 20%, 27%, 36%, 48%, 60%, and 74% at the scan rate of 0.2, 0.4, 0.6, 0.8, 1.0, and 2.0 mV s^{-1}, respectively. Notably, the capacitive-controlled contribution increased as the scan rate increased, due to the limited diffusion rate of the electrolyte ions into the interior of the electrode at high scan rate.

To further evaluate the practical application of the as-prepared $ZnCo_2O_4$ electrode, an asymmetric supercapacitor (ASC) was assembled by employing the as-prepared $ZnCo_2O_4$ as the positive electrode, AC as the negative electrode, and 6 M KOH as the electrolyte (Fig. 8a). The CV curves of the as-prepared $ZnCo_2O_4$ and the AC electrodes at the scan rate of 20 mV s^{-1} are shown in Fig. S3a.† The redox peaks of the as-prepared $ZnCo_2O_4$ electrode are corresponding to the typical reversible faradaic redox reactions, while the quasi-rectangle of the AC electrode confirms the characteristic electric double-layer capacitance. Fig. S3b† displays the CV curves of the ASC at different voltage windows at the scan rate of 20 mV s^{-1} to confirm the operating voltage window. Apparently, the CV curves are stable within 1.6 V. Whereas, the CV curves showed a slight hump and a distortion, which are ascribed to the irreversible reactions when the voltage window is higher than 1.6 V. Therefore, the optimum voltage window for the ASC is from 0 to 1.6 V. The CV curves of the ASC at different scan rates within a voltage window of 0 and 1.6 V are shown in Fig. 8b. Remarkably, the shape of CV curves is well maintained from 5 to 100 mV s^{-1}, indicating the fast discharging–charging properties of ASC. The GCD curves of the ASC at various current densities are shown in Fig. 8c. The discharge curves of the sample exhibited a plateau, which is consistent with the CV curves. The specific capacitance of the ASC is calculated from the corresponding GCD curves, and the results are plotted in Fig. 8d. The ASC delivered the specific capacitance values of 111.6, 101.9, 83.1, 66.0, and 56.9 F g^{-1} at the current densities of 0.5, 1, 2, 3, and 4 A g^{-1}, respectively. Furthermore, the cycling stability and coulombic efficiency of the ASC are carried out for 10 000 cycles at the current density of 1 A g^{-1}, as shown in Fig. 8e. The ASC shows good cycling stability with 71.4% specific capacitance retention of initial value after 10 000 cycles. The coulombic efficiency was maintained at nearly 100% during the 10 000 cycles. The Ragone plot of the ASC was used to describe the relationship between energy density and power density. Fig. 8f shows that the ASC can deliver a good energy density of 39.7 W h kg^{-1} at the power density of 400 W kg^{-1}, and the energy density still remains 20.2 W h kg^{-1} even at a high power density of 3200 W kg^{-1}. Such performance is superior to those of previous reported asymmetric supercapacitors, such as: OV-$ZnCo_2O_4$ nanosheets//AC (34.6 W h kg^{-1} at 160 W kg^{-1}),[16] $ZnCo_2O_4$@$Ni_xCo_{2x}(OH)_{6x}$//AC (26.2 W h kg^{-1} at 512 W kg^{-1}),[43] $ZnCo_2O_4$@$MnCo_2O_4$//AC (19.12 W h kg^{-1} at 750 W kg^{-1}),[44] $ZnCo_2O_4$ nanosheets//AC (20.3 W h kg^{-1} at 855 W kg^{-1}),[45] $ZnCo_2O_4$@$ZnWO_4$//AC (16.68 W h kg^{-1} at 2001 W kg^{-1}),[46] $ZnCo_2O_4$ NPs//MOF-NPC (18.0 W h kg^{-1} at 2500 W kg^{-1}),[47] $ZnCo_2O_4$ NPs//AC (16.0 W h kg^{-1} at 3580 W kg^{-1}).[15]

Furthermore, three ASCs connected in series can light up a blue light-emitting diode (LED) (2.0 V, 20 mA) for more than 25 min (Fig. S4†), indicating great potentials for practical applications of the assembled $ZnCo_2O_4$//AC ASC.

Table S2† shows a comparison between the as-prepared 3D hierarchical $ZnCo_2O_4$ nanosheets@nanowires films and the recent results reported in the literature, indicating that the material obtained in this work does exhibit excellent electrochemical properties. The superior electrochemical performance of the as-prepared 3D hierarchical $ZnCo_2O_4$ nanosheets@nanowires material is attributed to the following characteristics: firstly, the hierarchical porous architecture not only can facilitate the transportation of ions and electrons, but also buffer the volume changes and structural strain during the charge–discharge process, partially responsible for the enhanced cycling stability. Secondly, the free-standing structure can enhance the electric contact between the active material and the Ni foam substrate, thus reducing the contact resistance and improving the ion/electron diffusion. Thirdly, the synergistic effect of both 2D nanosheets and 1D nanowires in a 3D hierarchical micro/nanostructures not only provides a large surface area and sufficient active sites for redox reactions, but also possesses robust mechanical stability that can avoid self-aggregation during the repeated charge–discharge process. These features play a crucial role in ensuring the excellent electrochemical performance of the 3D hierarchical $ZnCo_2O_4$ nanosheets@nanowires electrode.

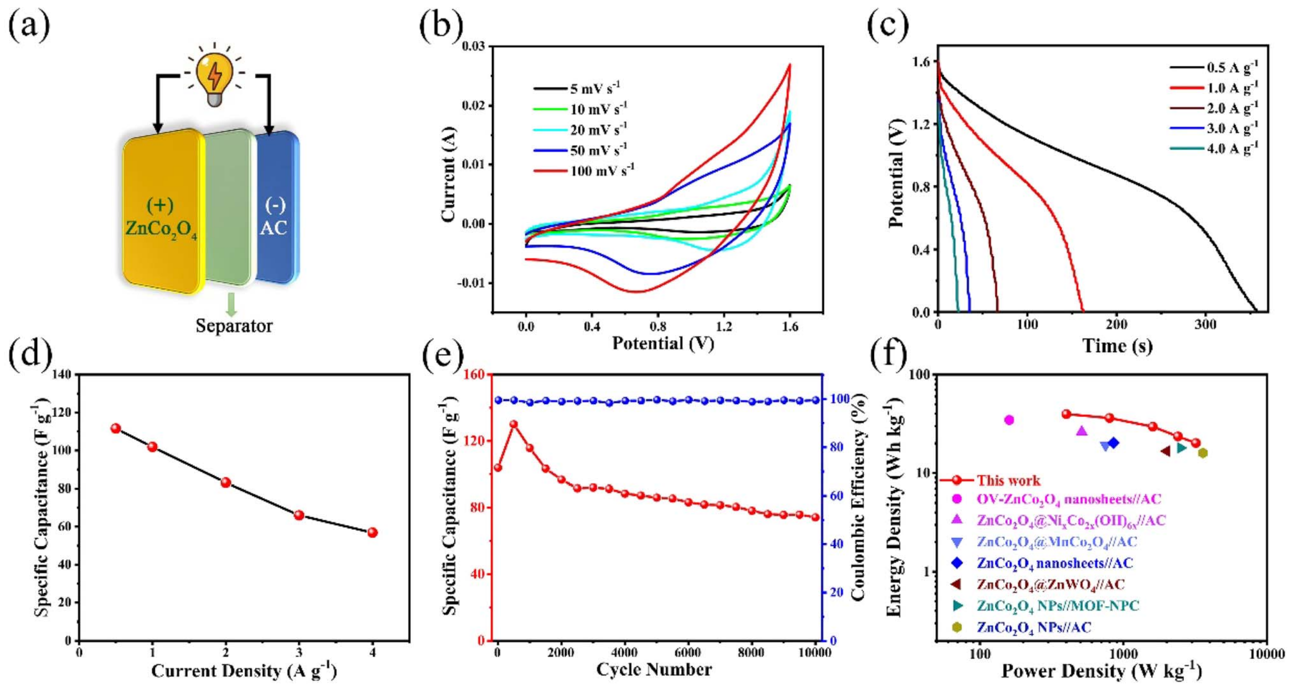

Fig. 8 Electrochemical performances of the as-assembled $ZnCo_2O_4$//AC ASC device. (a) Schematic illustration of the fabricated ASC device. (b) CV curves at different scan rates; (c) Galvanostatic discharge curves at different current densities. (d) Specific capacitance at different current densities. (e) Cycling stability and coulomb efficiency at a current density of 1 A g^{-1}. (f) Ragone plots of the ASC device and the previously reported devices.

4. Conclusions

We have successfully designed and developed a hydrothermal approach to synthesize controllably hierarchical porous 3D $ZnCo_2O_4$ nanosheets@nanowires films directly on Ni foam by simply tuning the amount of NH_4F as a morphology controlling agent. The effect of NH_4F on the morphologies and electrochemical properties has been systematically investigated and analyzed, finding that 40 mmol of NH_4F was the optimum concentration. Furthermore, the hierarchical porous 3D $ZnCo_2O_4$ nanosheets@nanowires electrode showed a prominent pseudocapacitive behaviour, demonstrating a high specific capacitance of 1289.6 F g^{-1} at 1 A g^{-1} and an excellent cycling stability with 86.8% capacity retention after 10 000 cycles at 1 A g^{-1}. In addition, the assembled $ZnCo_2O_4$//AC ASC delivered a remarkably high energy and power density as well as cycling stability. This is mainly attributed to its unique structure merits, including the large electroactive surface area, hierarchical porous architecture, free-standing structure, and robust mechanical stability. These attractive results demonstrate the great potentials of the hierarchically porous 3D $ZnCo_2O_4$ nanosheets@nanowires electrode for the next-generation high performance energy storage devices.

Author contributions

Huiqing Fan: conceptualization, project administration, funding acquisition, supervision, writing – original draft, writing – review & editing. Hexiang Di: conceptualization, methodology, formal analysis, writing – review & editing. Yanlei Bi: formal analysis, writing – review & editing. Ru Wang: formal analysis. Guangwu Wen: supervision. Lu-Chang Qin: supervision, validation, writing – review & editing.

Conflicts of interest

There are no conflicts to declare.

Acknowledgements

This work was financially sponsored by the Natural Science Foundation of Shandong Province (Grant No. ZR2019BB036).

References

1 B. Dunn, H. Kamath and J.-M. Tarascon, *Science*, 2011, **334**, 928–935.

2 A. C. Forse, C. Merlet, J. M. Griffin and C. P. Grey, *J. Am. Chem. Soc.*, 2016, **138**, 5731–5744.

3 P. Cai, J. Huang, J. Chen and Z. Wen, *Angew. Chem., Int. Ed.*, 2017, **129**, 4936–4939.

4 F. Wang, X. Wu, X. Yuan, Z. Liu, Y. Zhang, L. Fu, Y. Zhu, Q. Zhou, Y. Wu and W. Huang, *Chem. Soc. Rev.*, 2017, **46**, 6816–6854.

5 J. X. Zhao, Y. Zhang, X. X. Zhao, R. T. Wang, J. X. Xie, C. F. Yang, J. J. Wang, Q. C. Zhang, L. L. Li, C. H. Lu and Y. G. Yao, *Adv. Funct. Mater.*, 2019, **6**, 1900809.

6 S. Sun, J. Luo, Y. Qian, Y. Jin, Y. Liu, Y. Qiu, X. Li, C. Fang, J. Han and Y. Huang, *Adv. Energy Mater.*, 2018, **8**, 1801080.
7 S. W. Zhang, B. S. Yin, X. X. Liu, D. M. Gu, H. Gong and Z. B. Wang, *Nano Energy*, 2019, **59**, 41–49.
8 Y. Shao, M. F. El-Kady, J. Sun, Y. Li, Q. Zhang, M. Zhu, H. Wang, B. Dunn and R. B. Kaner, *Chem. Rev.*, 2018, **118**, 9233–9280.
9 T. T. Liu, S. Zhou, X. H. Yu, C. Mao, Y. J. Wei, X. Y. Yu, L. Chen, X. Zhao, G. X. Tian and L. Chen, *RSC Adv.*, 2022, **12**, 4029–4041.
10 X. Zhao, L. Mao, Q. Cheng, J. Li, F. Liao, G. Yang, L. Xie, C. Zhao and L. Chen, *Chem. Eng. J.*, 2020, **387**, 124081.
11 S. H. Zhao, X. B. Yu, H. M. Chen, K. Tao, Y. P. Hua and L. Han, *RSC Adv.*, 2020, **10**, 13922–13928.
12 B. Liu, Q. Wang, X. Wang, D. Chen and G. Shen, *ACS Appl. Mater. Interfaces*, 2013, **5**, 10011–10017.
13 S. B. Wang, J. Pu, Y. Tong, Y. Y. Cheng, Y. Gao and Z. H. Wang, *J. Mater. Chem. A*, 2014, **2**, 5434–5440.
14 G. Koyyada, N. S. Kumar, I. H. A. Ghurabi, M. Boumaza, J. H. Kim and K. Mallikarjuna, *RSC Adv.*, 2021, **11**, 5928–5937.
15 J. Bhagwan, S. K. Hussain and J. S. Yu, *J. Alloys Compd.*, 2020, **815**, 152456.
16 K. Xiang, D. Wu, Y. Fan, W. You, D. Zhang, J. L. Luo and X. Z. Fu, *Chem. Eng. J.*, 2021, **425**, 130583.
17 W. L. Bai, H. Tong, Z. Z. Gao, S. H. Yue, S. H. Xing, S. Y. Dong, L. F. Shen, J. P. He, X. G. Zhang and Y. Y. Liang, *J. Mater. Chem. A*, 2015, **3**, 21891–21898.
18 C. Wu, J. Cai, Q. Zhang, X. Zhou, Y. Zhu, L. Li, P. Shen and K. Zhang, *Electrochim. Acta*, 2015, **169**, 202–209.
19 V. Venkatachalam, A. Alsalme, A. Alswieleh and R. Jayavel, *Chem. Eng. J.*, 2017, **321**, 474–483.
20 C. Y. Du, E. S. Han, L. M. Sun, S. P. Qiao and L. N. Li, *Ionics*, 2020, **26**, 383–391.
21 H. Chen, J. Wang, X. Han, F. Liao, Y. Zhang, L. Gao and C. Xu, *Ceram. Int.*, 2019, **45**, 8577–8584.
22 K. W. Qiu, Y. Lu, D. Y. Zhang, J. B. Cheng, H. L. Yan, J. Y. Xu, X. M. Liu, J. K. Kim and Y. S. Luo, *Nano Energy*, 2015, **11**, 687–696.
23 Z. Dai, Z. Long, R. Li, C. Shi, H. Qiao, K. Wang and K. E. Liu, *ACS Appl. Energy Mater.*, 2020, **3**, 12378–12384.
24 M. Tortosa, F. J. Manjon, M. Mollar and B. Mari, *J. Phys. Chem. Solids*, 2012, **73**, 1111–1115.
25 W. Q. Ma, H. H. Nan, Z. X. Gu, B. Y. Geng and X. J. Zhang, *J. Mater. Chem. A*, 2015, **3**, 5442–5448.
26 H. Q. Liu, D. P. Zhao, Y. Liu, Y. L. Tong, X. Wu and G. Z. Shen, *Sci. China Mater.*, 2021, **64**, 581–591.
27 C. S. Pan, R. X. Zhang, R. G. Nuzzo and A. A. Gewirth, *Adv. Energy Mater.*, 2018, **8**, 1800589.
28 D. P. Zhao, M. Z. Dai, H. Q. Liu, L. Xiao, X. Wu and H. Xia, *Cryst. Growth Des.*, 2019, **19**, 1921–1929.
29 S. Kulesza and M. Bramowicz, *Appl. Surf. Sci.*, 2014, **293**, 196–201.
30 Y. Chen, B. Qu, L. Hu, Z. Xu, Q. Li and T. Wang, *Nanoscale*, 2013, **5**, 9812–9820.
31 Q. Yang, Z. Lu, Z. Chang, W. Zhu, J. Sun, J. Liu, X. Sun and X. Duan, *RSC Adv.*, 2012, **2**, 1663–1668.
32 J. Jiang, J. P. Liu, X. T. Huang, Y. Y. Li, R. M. Ding, X. X. Ji, Y. Y. Hu, Q. B. Chi and Z. H. Zhu, *Cryst. Growth Des.*, 2010, **10**, 70–75.
33 X. Wu, X. Han, X. Ma, W. Zhang, Y. Deng, C. Zhong and W. Hu, *ACS Appl. Mater. Interfaces*, 2017, **9**, 12574–12583.
34 S. Y. Zeng, R. F. Tang, S. X. Duan, L. Li, C. H. Liu, X. L. Gu, S. S. Wang and D. Z. Sun, *J. Colloid Interface Sci.*, 2014, **432**, 236–245.
35 X. W. Lou, C. Yuan, E. Rhoades, Q. Zhang and L. A. Archer, *Adv. Funct. Mater.*, 2006, **16**, 1679–1684.
36 J. Liu, X. Huang, Y. Li, X. Ji, Z. Li, X. He and F. Sun, *J. Phys. Chem. C*, 2007, **111**, 4990–4997.
37 G. Q. Zhang, H. B. Wu, H. E. Hoster, M. B. Chan-Park and X. W. Lou, *Energy Environ. Sci.*, 2012, **5**, 9453–9456.
38 Y. Zhu, Z. Wu, M. Jing, X. Yang, W. Song and X. Ji, *J. Power Sources*, 2015, **273**, 584–590.
39 Y. Shang, T. Xie, C. Ma, L. Su, Y. Gai, J. Liu and L. Gong, *Electrochim. Acta*, 2018, **286**, 103–113.
40 S. Nagamuthu, S. Vijayakumar and G. Muralidharan, *Energy Fuels*, 2013, **27**, 3508–3515.
41 M. Z. Dai, H. Q. Liu, D. P. Zhao, X. F. Zhu, X. Wu and B. Wang, *ACS Appl. Energy Mater.*, 2021, **4**, 2637–2643.
42 B. Q. Hou, X. Jin, L. L. Jiang, Y. H. Li, C. J. Qiu, D. D. Han, Y. S. Ding and L. Z. Sheng, *Appl. Surf. Sci.*, 2021, **569**, 151036.
43 W. Fu, Y. Wang, W. Han, Z. Zhang, H. Zha and E. Xie, *J. Mater. Chem. A*, 2016, **4**, 173–182.
44 L. Wang, Y. Guan, X. Zhao, J. Mu, H. Che, H. Li and Z. Guo, *J. Mater. Sci.: Mater. Electron.*, 2018, **29**, 5782–5790.
45 Y. Zhou, L. Chen, Y. Jiao, Z. Li and Y. Gao, *Electrochim. Acta*, 2019, **299**, 388–394.
46 L. Xie, Y. Liu, H. Bai, C. Li, B. Mao, L. Sun and W. Shi, *J. Colloid Interface Sci.*, 2018, **531**, 64–73.
47 D. He, Y. Gao, Y. Yao, L. Wu, J. Zhang, Z. H. Huang and M. X. Wang, *Front. Chem.*, 2020, **8**, 719.